Proceedings of the Twenty-sixth (2016) International Ocean and Polar Engineering Conference **www.isope.org**
Rhodes, Greece, June 26-July 1, 2016

ISBN 978-1-880653-88-3; ISSN 1098-6189

Algorithms for tsunami detection by High Frequency Radar : development and case studies for tsunami impact in British Columbia, Canada

Stéphan T. Grilli[1]*, Michael Shelby*[1]*, Annette Grilli*[1]*, Charles-Antoine Guérin*[2]*, Samuel Grosdidier*[3] *and Tania Insua*[4]
(1) Department of Ocean Engineering, University of Rhode Island, Narragansett, RI, USA
(2) Université de Toulon, CNRS, Aix Marseille Université, IRD MIO UM 110, La Garde, France
(3) Diginext Ltd., Toulouse, France
(4) Ocean Networks Canada (ONC), Victoria, BC, Canada

ABSTRACT

A shore-based High-Frequency (HF) WERA radar was recently installed by Ocean Networks Canada (ONC) near Tofino, British Columbia (Canada), to mitigate the elevated tsunami hazard along the shores of Vancouver Island, from both far- and near-field seismic sources and, in particular, from the Cascadia Subduction Zone (CSZ). With this HF radar, ocean currents can be measured up to a 70-85 km range, depending on atmospheric conditions, based on the Doppler shift they cause in ocean waves at the radar Bragg frequency. In earlier work, the authors (and others) have shown that tsunami currents need to be at least 0.15-0.20 m/s to be reliably detectable by HF radar, when considering environmental noise and background currents (from tide and mesoscale circulation). This would limit the direct detection of tsunami-induced currents to shallow water areas where they are sufficiently strong due to wave shoaling and, hence, to the continental shelf. It follows that, in locations with a narrow shelf, warning times based on such a tsunami detection method may be small.

To detect tsunamis in deeper water, beyond the shelf, the authors have proposed a new algorithm that does not require "inverting" currents, but instead is based on spatial correlations of the raw radar signal at two distant locations/cells located along the same wave ray, time shifted by the tsunami propagation time along the ray. A pattern change in these correlations indicates the presence of a tsunami. They validated this algorithm for idealized tsunami wave trains propagating over a simple seafloor geometry in a direction normally incident to shore. Here, this algorithm is further developed, extended, and validated for realistic case studies conducted for seismic tsunami sources and using the bathymetry, offshore of Vancouver Island, BC. Tsunami currents, computed with a state-of-the-art long wave model, are spatially averaged over cells aligned along individual wave rays, within the radar sweep area, obtained by solving the wave geometric optic equation. A model simulating ONC radar's backscattered signal in space and time, as a function of the simulated tsunami currents, is applied on the Pacific Ocean side of Vancouver Island. Numerical experiments are performed, showing that the proposed algorithm works for detecting a realistic tsunami. Correlation thresholds relevant for tsunami detection can be inferred from the results.

INTRODUCTION

Major tsunamis can be enormously destructive and cause large numbers of fatalities along the world's increasingly populated and developed coastlines (Ioualalen et al., 2007; Grilli et al., 2013). While the brunt of tsunami impact cannot be easily attenuated, loss of life, however, can be mitigated or even eliminated by providing early warning to coastal populations. Such warnings can be issued based on early detection and assessment of the mechanisms of tsunami generation (e.g., seismicity) as well as detection of the tsunami itself as soon as possible after its generation. The latter is particularly important when the tsunami source is located close to the nearest coastal areas, and thus both energy spreading is low and propagation time is short. This is the case, for instance for co-seismic tsunamis generated in nearshore subduction zones (SZ) (e.g., Japan Trench, Puerto Rico Trench, Cascadia SZ,...), or for submarine mass failures (SMFs), that can be triggered on or near the continental shelf slope by moderate seismic activity (Fine et al., 2005; Tappin et al., 2008; Grilli et al., 2015b); meteotsunamis, also, may be generated on continental shelves by fast moving elongated low pressure systems (e.g., derechos) (Thomson et al., 2009).

The detection of offshore propagating tsunamis from a nearshore generation area is usually made in deep water, at bottom-mounted pressure sensors (so-called DART buoys), based on which a warning is issued for far-field locations. The detection of onshore propagating tsunamis in shallow water, over the continental shelf, is typically made by bottom pressure sensors and tide gauges that may not survive the impact of large tsunamis; additionally such detection is local (i.e., point-based) and often takes place too late (i.e., too close to shore) to be used in early warning systems. Hence, with the current detection technology used in tsunami warning systems, there may not be enough time to issue a warning for near-shore seismic or SMF tsunami sources, based on actual tsunami data. When the earthquake is the tsunami triggering mechanism, a warning can be issued based on detecting seismic waves and from these estimating the earthquake parameters and the likelihood for tsunami generation. For non-seismically induced nearshore SMF tsunamis or for meteotsunamis, a warning can only be issued based on detecting the tsunami at nearshore sensors and, hence, there may not even be enough time to issue it before the tsunami impacts the coast; this is particularly more so in the case of a narrow shelf.

Grid	SW corner (Lat/Lon)	N_x x N_y grid cells	Resolution (actual)	Resolution ($\sim$ m)
G0	(10.00,-180.00)	1950 x 1560	0.6 min (S)	3,600
G1	(44.00,-129.01)	700 x 600	2 min (S)	1,089
G2	(46.99, -127.52)	766 x 900	270 m (C)	270
G3	(48.25, -126.90)	1800 x 1200	90 m (C)	90

Table 1: Parameters of nested grids in FUNWAVE-TVD simulations, in which G0 is a spherical (S) grid with 100 km thick sponge layers on the outside boundary, and G1, G2 and G3 are spherical (S) or Cartesian (C) grids centered on the WERA radar sweep area in Tofino, BC (Figs. 1a and 2a). G1-G3 simulations are performed by one-way coupling.

The use of shore-based High Frequency (HF) radars to detect incoming tsunami waves has been proposed almost 40 years ago by Barrick (1979) and, more recently, was supported by numerical simulations (see, e.g., Lipa et al. (2006), Heron et al. (2008), Dzvonkovskaya et al. (2009), Gurgel et al. (2011)), and by HF radar measurements made during the Tohoku 2011 tsunami in Japan (Hinata et al., 2011; Lipa et al., 2011, 2012), in Chile (Dzvonkovskaya, 2012), and in Hawaii (Benjamin et al., 2016). No realtime tsunami detection algorithms were in place, but an a posteriori analysis of the radar data identified the tsunami current in the measurements. As for other nearshore currents, this works by measuring the Doppler shift tsunami currents induce on the radar signal and from this estimating time series of radial surface currents (i.e., projected on the radar line-of-sight) over a grid of radar cells covering the radar sweep area (typical cell size is one to a few km in each direction, with10th to 100th of km in the radial direction, depending on radar frequency and power). This dense spatial coverage is another advantage of HF radar detection over standard instrument methods. Tsunami detection and warning algorithms were proposed in some of these earlier studies, based on both a sufficient magnitude of the tsunami current inferred from the radar Doppler spectrum, combined with identifying its oscillatory nature in space and time. In earlier work based on a 4.5 MHz HF radar (Stradivarius) with a 200 km range, Grilli et al. (2015a) showed that such algorithms reliably work when tsunami currents are at least $U_t \sim 0.15 - 0.20$ m/s, and thus raise above background noise and currents. Hence, this limits a direct detection of tsunami currents to fairly shallow water and thus nearshore locations, and also means short warning times, unless there is a very wide shelf.

To detect a tsunami in deeper water, beyond the continental shelf, the authors proposed a new detection algorithm that does not require "inverting" currents, but instead is based on computing spatial correlations of the raw radar signal at pairs of radar cells located along the same wave ray, shifted in time by the tsunami propagation time along the ray. A change in pattern of these correlations indicates an approaching tsunami, since no other geophysical phenomenon can be responsible. They validated this algorithm only for idealized tsunami wave trains, propagating over a simple seafloor geometry in a direction normally incident to shore (Grilli et al., 2015a). Here, this algorithm is extended and validated for the area offshore of Vancouver Island, in British Columbia (Canada), based on realistic tsunami case studies conducted for seismic sources. To mitigate tsunami hazard in this area from both far- and near-field seismic sources, in particular, from the Cascadia Subduction Zone (CSZ), Ocean Networks Canada (ONC) recently installed a shore-based WERA HF radar near Tofino (TF), BC. This HF radar can remotely sense ocean currents up to a 70-85 km range, depending on ocean/atmospheric conditions (Fig. 1b). In this paper, we perform numerical experiments to confirm that the proposed algorithm also works for a site with complex bathymetry and for realistic tsunami data; results will allow defining correlation thresholds relevant for tsunami detection. In the numerical experiments, tsunami currents are computed with the state-of-the-art long wave model FUNWAVE-TVD (Shi et al., 2012; Kirby et al., 2013a) and spatially averaged over a series of radar cells aligned along individual wave rays, obtained by solving the geometric optic equation. Here, we only detail results for a M_w 9.1 far-field seismic source located in the Semidi Subduction zone (SSZ; Fig. 1a), but simulations were also performed for large seismic sources in the CSZ (Insua et al., 2015). The radar signal is simulated in each cell based on the computed time series of tsunami radial currents using a backscattering model (Grilli et al., 2015a), which is applied for the characteristics of the WERA radar installed in TF (carrier electromagnetic wave (EMW) frequency $f_{EM} = 13.5$ MHz). This is detailed in the following sections.

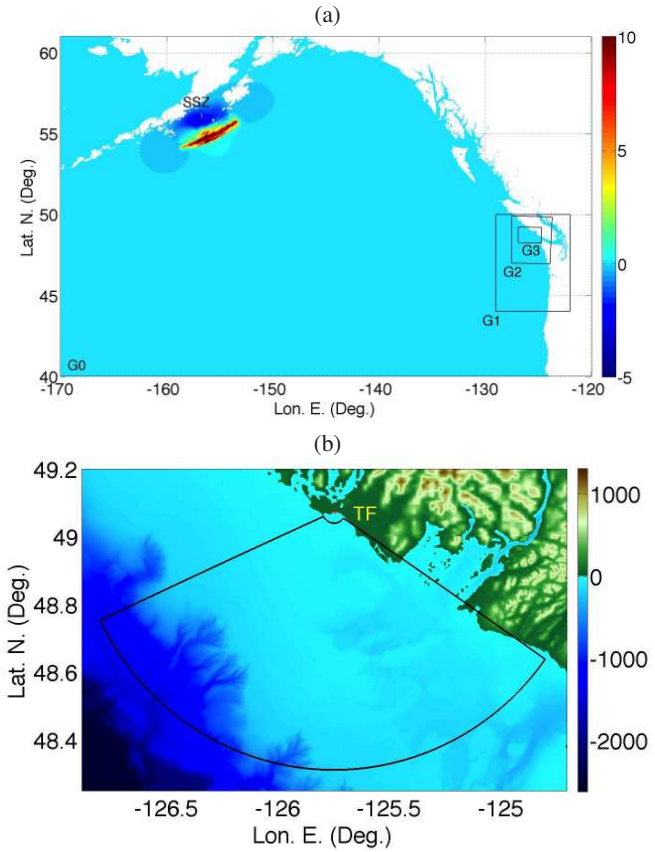

Fig. 1: (a) Zoom-in on Pacific Ocean area covered by 2 arc-min grid G0, with initial surface elevation (color scale in meter) of the M_w 9.1 SAFRR seismic source in the Semidi Subduction Zone (SSZ), and boundary of nested model grids G1 (0.6 arc-min), G2 (270 m), and G3 (90 m) around Vancouver Island, BC) (Table 1). (b) Zoom-in on area of grid G3 around the WERA HF radar deployment site in Tofino (TF); the thick black line marks the measurement (sweep) area (85 km radius) covered by the radar (color scale is bathymetry (< 0) and topography (> 0) in meter).

TSUNAMI SIMULATIONS

Numerical models, tsunami source and numerical grids

We extend a HF radar simulator and tsunami detection algorithm proposed earlier by Grilli et al. (2015a), and apply both to the sweep area of the WERA radar, off of Tofino, BC, based on simulated tsunami currents corresponding to the arrival of a tsunami generated by a M_w 9.1 seismic source in the SSZ (Fig. 1). This source was designed by the SAFRR (Science Application for Risk Reduction) group to have the same magnitude as the Tohoku 2011 event and cause maximum impact in northern California (Kirby et al., 2013b). Simulations of tsunami propagation are performed with FUNWAVE-TVD, a Boussinesq long wave model with extended dispersive properties, which is fully nonlinear in Cartesian

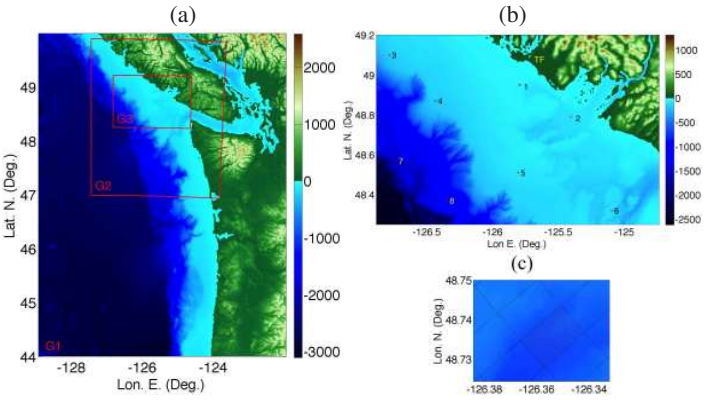

Fig. 2: Tsunami simulations with FUNWAVE-TVD off of Vancouver Island, BC: (a) Details of nested grids G1, G2 and G3 (Fig. 1a; Table 1) centered on Tofino, BC; (b) Area of grid G3 with numbered locations of numerical wave gauge stations; and (c) Zoom-in onto radar cell mesh in radar sweep area (Figs. 1b, 3), with marked locations (red dots) of G3 grid cells contained in one radar cell. [Color scale and contours is bathymetry (<0) and topography (>0) in meter.]

grids (Shi et al., 2012) and weakly nonlinear in spherical grids (Kirby et al., 2013a). This model was efficiently parallelized for use on a shared memory cluster (over 90% scalability is typically achieved), which allows using large grids (such as here the G0 grid, which has over 3 million grid cells, as detailed below). FUNWAVE (its earlier version) and FUNWAVE-TVD have been widely used to simulate tsunami case studies (Grilli et al., 2007, 2010, 2013, 2015b; Ioualalen et al., 2007; Tappin et al., 2008, 2014; Abadie et al., 2012; Tehranirad et al., 2015). Since 2010, the authors have used this model and related methodology to compute tsunami inundation maps for the US East Coast, under the auspice of the US National Tsunami Hazard Mitigation Program (NTHMP) (see work and maps reported at: http://chinacat.coastal.udel.edu/nthmp.html). Both spherical and Cartesian versions of FUNWAVE-TVD were validated through benchmarking and approved for NTHMP work (Tehranirad et al., 2011).

The initial surface elevation of the SAFRR seismic source was obtained from Kirby et al. (2013b) (source labeled "KirbyAlaskaPeninsulaTotal"; see http://atom.giseis.alaska.edu) and used as initial condition in FUNWAVE-TVD, with zero velocity (Fig. 1a). Four levels of nested grids were used in the simulations, with the coarser one G0, a 2 arc-min resolution spherical coordinate grid, covering a large area of the Pacific Ocean, and G1, G2, and G3 being spherical and Cartesian nested grids centered on Tofino, BC, with higher resolutions of 0.6 arc-min (1,089 m), 270 m, and 90 m (Figs. 1a and 2a). Table 1 provides parameters for each grid, including numbers of grid cells. To eliminate reflection, 100 km thick sponge layers are used along the outside boundary of grid G0. Simulations in finer nested grids are performed by one-way coupling. In this method, time series of surface elevation and depth-averaged current are computed for a large number of stations/numerical wave gauges defined within a coarser grid, along the boundary of the finer grid used in the next level of nesting. Computations are fully performed in the coarser grid and then restarted in the finer grid using the station time series as boundary conditions. As these include both incident and reflected waves computed in the coarser grid, this method closely approximates open boundary conditions. It was found that a nesting ratio with a factor 3-4 reduction in grid size allowed achieving good accuracy in tsunami simulations, which is the case for grids used here (Table 1).

Bathymetric/topographic data for both the 2 arc-min resolution G0 grid and the 0.6 arc-min G1 grid was interpolated from NOAA's 1 arc-min ETOPO-1 data. Bathymetry for the 270 m and 90 m resolution grids (G2 and G3) was based on the 3 arc-sec data provided for the coast of BC by NOAA's Marine Geology and Geophysics (MGG), wherever available. This higher-resolution data was also used in grids G0 and G1, instead of ETOPO-1 data, in the area overlapping with grid G2. Another MGG 3 arc-sec dataset (the Northwest Pacific data set) was used for areas facing the US coast not covered by the BC bathymetry. Since the MGG BC dataset only included bathymetry, topography for grids G2 and G3 was based on ETOPO-1 data, which clearly is too coarse to accurately simulate coastal tsunami impact in these finer grids. This however is acceptable, since the present work focuses on detecting the tsunami offshore, at a significant distance away from the shoreline.

Offshore of shallow nearshore areas, tsunamis are long waves that are well described by linear wave theory (Dean and Dalrymple, 1984). Hence, tsunami currents and elevations can be estimated as,

$$\boldsymbol{U}_t \simeq \eta_t \sqrt{\frac{g}{h}}\frac{\boldsymbol{k_t}}{k_t} \quad \text{and} \quad \eta_t \simeq \eta_{t0}\left\{\frac{c_0(h_0)}{c(h)}\right\}^{\frac{1}{2}} = \eta_{t0}\left\{\frac{h_0}{h}\right\}^{\frac{1}{4}} \tag{1}$$

respectively, where $\eta_t \ll h(x,y)$ (the local depth) is surface elevation at location (x,y), $k_t(x,y) = |\,\boldsymbol{k_t}\,| = 2\pi/L_t$ is the tsunami wavenumber (with $L_t \gg 20h$ the characteristic tsunami wave length, and thus steepness $\eta_t/L_t \ll 1$), and $\boldsymbol{k_t} = k_t(\cos\phi_t, \sin\phi_t)$ is the wavenumber vector, with ϕ_t the angle of the tsunami local direction of propagation with respect to the x axis ($g = 9.81$ m/s^2, is gravitational acceleration). According to Eq. (1), assuming no refraction and linear long waves, the local tsunami elevation η_t can be predicted based on the initial deep water tsunami elevation η_{t0} using Green's law, where $c_0 = \sqrt{gh_0}$ is the tsunami phase speed in reference depth h_0. It follows that $|\,\boldsymbol{U}_t\,| = U_t \propto h^{-3/4}$, and the tsunami current gradually increases as water depth decreases.

As detailed in Grilli et al. (2015a), the proposed HF radar detection algorithm is applied along individual wave rays, which are function of site specific wave refraction. These can be pre-computed for a specified bathymetry $h(x,y)$ independently of tsunami sources, given the rays' assumed incident direction in deep water ϕ_{t0}, using the geometric optics eikonal equation (Dean and Dalrymple, 1984). Using the long wave celerity (equal to the group velocity) it reads,

$$\frac{\partial \phi_t}{\partial x} + \left\{1 - \frac{1}{2h}\frac{\partial h}{\partial x}\right\}\tan\phi_t \frac{\partial \phi_t}{\partial y} + \frac{1}{2h}\frac{\partial h}{\partial y} = 0 \tag{2}$$

and is solved for $\phi_t(x,y)$, the local ray angle.

The pre-computed wave rays allow identifying radar cells located along the same ray (see details in next section); the tsunami propagation time between each pair of such cells (p,q) is then calculated as,

$$\Delta t_{pq} = t(\boldsymbol{R}_q) - t(\boldsymbol{R}_p) = \oint_{s(\boldsymbol{R}_p)}^{s(\boldsymbol{R}_q)} \frac{\mathrm{d}s}{\sqrt{gh(s)}} \tag{3}$$

where $\boldsymbol{R}(x,y)$ denotes the radial position of cells in the radar grid and $s(\boldsymbol{R}(x,y))$ is the curvilinear abscissa along the selected wave ray, with $\mathrm{d}s = \mathrm{d}x\cos\phi_t + \mathrm{d}y\sin\phi_t$.

Tsunami simulation results

Figure 3 shows the maximum surface elevations computed during simulations in grid G0 (a) and G3 (b) for the SAFRR seismic source in the SSZ (Fig. 1a). As expected, Fig. 3a shows energy focusing on northern California and Oregon; however, one can also see significant tsunami elevations near Tofino. This is clearer in Fig. 3b, which shows that this tsunami would cause maximum elevations/runup of at least 2 m near Tofino. For the same case, Fig. 4a shows time series of surface elevation computed at 8 stations/numerical gauges located on the shelf off of Tofino (see locations in Fig. 2b). Each sub-figure in Fig. 4a compares results obtained at the same gauge in grids G2 and G3, showing a good

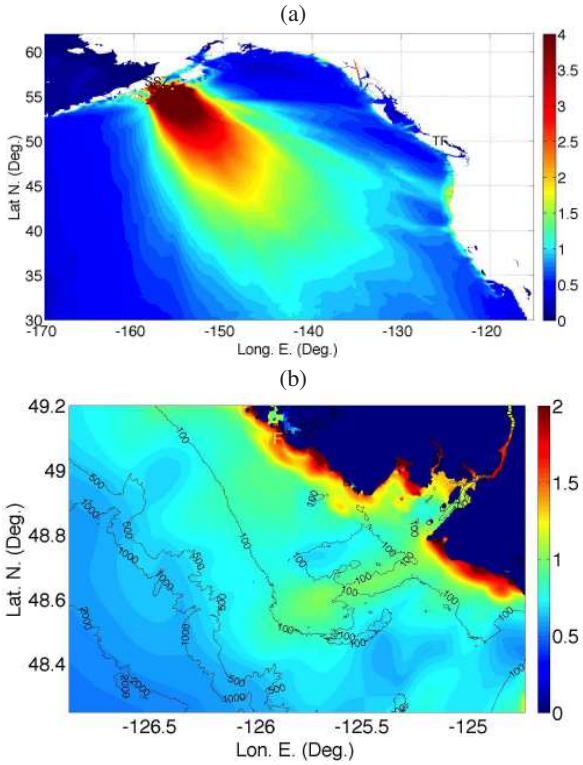

Fig. 3: Simulations with FUNWAVE-TVD of M_w 9.1 SAFRR seismic source in SSZ (Fig. 1a). Maximum surface elevation (color scale in meter) during simulations in grids (Fig. 1): (a) G0 (only zoom-in area is shown); and (b) G3. TF marks HF radar deployment site in Tofino, BC.

agreement of the one-way coupling results for the incident tsunami; the agreement is less good once reflected waves have propagated back to the stations, as the interaction of waves with the coastline (including dissipation by breaking and bottom friction) is less accurately modeled in the coarser grid. At the two stations closest to shore near Tofino (stations 1 and 2), the incident tsunami height is over 2 m (trough to crest).

Figure 5a shows examples of wave rays computed by solving Eq. (2) for the bathymetry in grid G3, offshore of Tofino (Fig. 2), assuming incident directions from west or southwest ($\phi_{t0} = 0$ or 45 deg); as expected, wave rays bend based on bathymetry to become increasingly normal to bathymetric contours in shallower water close to shore. For this reason, wave rays initially incident from different directions in deeper water end up being quite similar in shallower water, which implies that the same wave rays selected over the radar sweep area can be used for various incident tsunami (and source) directions. Figure 4b shows time series of tsunami radial currents (i.e., projected in the radar direction $U_{tr} = \boldsymbol{U}_t \cdot \boldsymbol{R}/R$) computed at the locations of 9 radar cells numbered 1-9 along a specific wave ray, in increasingly deeper water (Fig. 5b). As expected from Eq. (1), while radial velocity is over 0.4 m/s in the shallower water cell (1) in less than 50 m depth, it is less than 0.07 m/s at the deeper cell (9) close to the shelf break, in 500 m depth. The figure also shows that, independently of its magnitude, the pattern of time variation of the tsunami current repeats itself well from station 9 to 1. This is even more apparent in Fig. 4c where the same time series have been time- shifted by the long wave propagation time t_{p1} computed from cell $p = 2, ..., 9$ to cell 1 using Eq. (3). As we shall see, such time-shifted currents are highly correlated in time, which was one of the main conclusions in the earlier work by Grilli et al. (2015a), based on both idealized tsunami wave train and bathymetry. It thus appears from results tin Fig. 4 that this key property of tsunami currents for the viability of the proposed detection algorithm is confirmed for a more realistic tsunami case study.

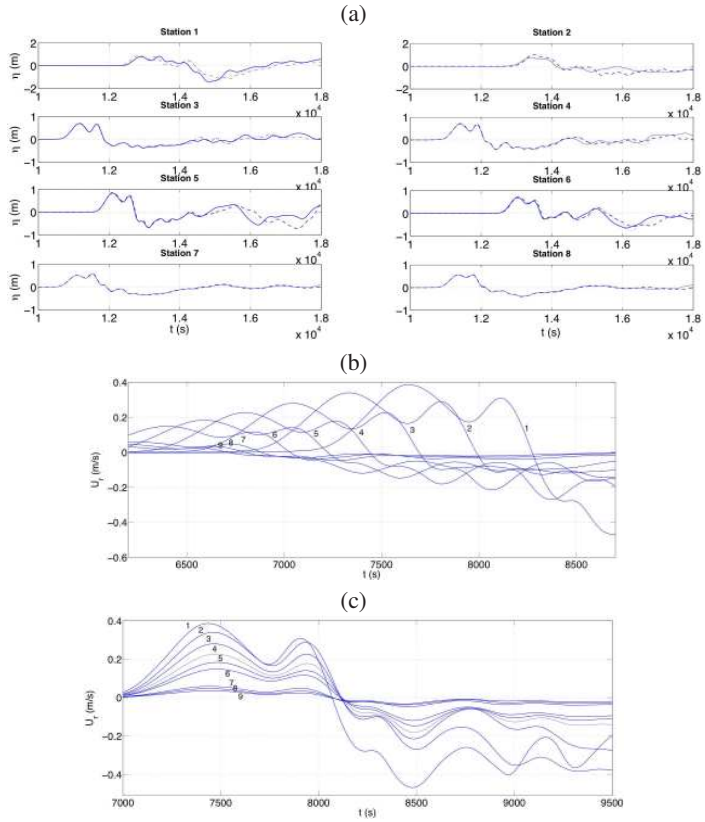

Fig. 4: Time series of (a) surface elevation at stations 1-8 (Fig. 2b) in grid G2 (dash lines) and G3 (solid lines); (b,c) spatially-averaged radial current velocity U_r in radar cells 1-9 aligned along a given wave ray (Fig. 5b): (b) as a function of time; (c) shifted in time by the long wave propagation time t_{p1} from cell $p = 2, ..., 9$ to cell 1.

SIMULATIONS OF TSUNAMI DETECTION BY HF RADAR

HF radar detection of tsunami currents

To simulate tsunami detection by HF radar, based on radial currents U_{tr} computed with FUNWAVE-TVD (e.g., Fig. 4), we use the HF radar simulator model developed and validated by Grilli et al. (2015a); background information on the detection of coastal currents by HF radar can be found in this reference. Parameters of the simulator were set to match the characteristics of the WERA radar deployed near Tofino, BC, which has a carrier electromagnetic wave (EMW) frequency $f_{EM} = 13.5$ MHz and a usable maximum range of 85 km. The radar sweep area is outlined in Fig. 1a and detailed in Fig. 5b; it is covered by radar cells within which the received radar signal is averaged, of length $\Delta R = 1.5$ km in the radial direction and angular opening $\Delta\phi_r = 1$ degree in the azimuthal direction; the detection sector of the sweep area is 120 degree, implying that cells are 1.48 km wide at a 85 km range and narrower closer to the radar (cell area: $\Delta\mathbb{S} = R\Delta R\Delta\phi_r$ increases with range). [The orientation of the radar array of 12 antennas (275 deg. from N, clockwise; centered at 49° 4' 24.82" N, 125° 46' 11.55" W) is such that one side of the sweep area boundary is nearly parallel to the coastline southeast of Tofino (Fig. 5b), and its length (110 m) allows for the 1 deg azimuthal resolution.]

Near-surface ocean currents are inferred from EMW interactions with ocean surface waves based on the Bragg scattering property that the diffracted radar signal is maximum when it interacts with ocean waves whose wavelength L_B is half the EWM wavelength. Thus,

$$L_B = \frac{\lambda_{EM}}{2} = \frac{gT_B^2}{2\pi} \quad \text{with} \quad \lambda_{EM} = \frac{c_{EM}}{f_{EM}}; \quad \text{and} \quad f_B = \sqrt{\frac{g f_{EM}}{\pi c_{EM}}} \tag{4}$$

with $c_{EM} = 299,700$ km/s the speed of light in the air and f_B the Bragg

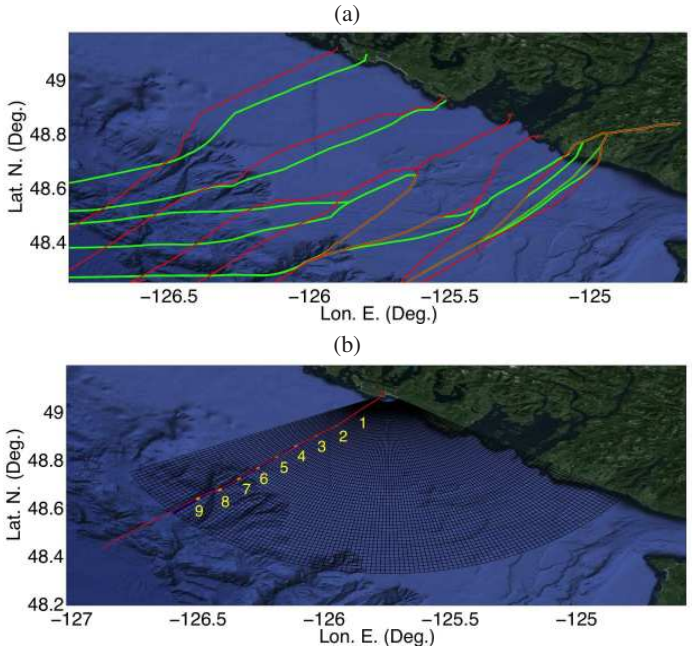

Fig. 5: (a) Examples of wave rays computed from incident directions from west (green; $\phi_{t0} = 0$ deg) and southwest (red; $\phi_{t0} = 45$ deg), as a function of bathymetry in grid G3, over the Tofino WERA HF radar sweep area (Fig. 2); (b) Radar cell grid with one selected wave ray (red line) intersecting the grid, and nine intersected cells numbered 1-9 as a function of increasing radar range and water depth.

frequency. For the WERA radar, we find $L_B \simeq 11.1$ m; assuming deep water ocean waves, the first Eq. (4) further yields the wave period, $T_B = 2.66$ s and $f_B = 0.375$ Hz. Based on a Pierson Moskowitz spectrum, wind waves of this period and length are present in the ocean for low wind speeds (at a 10 m elevation), $U_{10} \geq 0.318\sqrt{gL_B} = 3.3$ m/s (or 6.5 knots); hence, they are widespread.

Tsunami radial currents U_{tr} cause Doppler effects on ocean waves, which shift the Bragg frequency in the radar signal Doppler spectrum by, $\Delta f_B = \pm \mid U_{tr} \mid /L_B$, depending on current sign. The magnitude of radial currents, $\overline{\tilde{U}_{tr}}(\boldsymbol{R},t)$ can thus be inferred (inverted) from these shifts once the radar signal Doppler spectrum is computed; these are currents averaged (overbar) over a radar cell of area $\Delta\mathbb{S}$ (for a monostatic configuration such as here), centered at $\boldsymbol{R}(x,y)$, and a measuring (or integration) time interval T_i (tilde) (here 120 s). To accurately compute the spectrum, the radar cells' spatial dimensions must be sufficiently large to include a statistically meaningful sample of ocean surface waves of various wavelengths, and particularly of length L_B. The frequency resolution of the Doppler spectrum near its peak is, $\Delta f_D = 1/T_i$ and that of the inverted current $\Delta U_{tr} = L_B/T_i$. Hence, to accurately infer surface currents based on a Doppler shift, the measuring time interval must be sufficiently long, typically at least 2 min for a 13.5 MHz (such as used here), yielding $\Delta U_{tr} = 0.086$ m/s. Because of the oscillatory nature of tsunami currents, however, T_i cannot be increased too much to improve resolution, as this would gradually reduce the cell- and time-averaged currents, until they have a nearly zero average and become undetectable. As concluded by Grilli et al. (2015a), the limited resolution of inverted currents combined with their rapidly decreasing magnitude with radar range (and increasing depth (Eq. (1)) implies that tsunami detection algorithms, such as proposed by Lipa et al. (2012), based on "inverting" Doppler spectral shifts would only be reliable nearshore, over the continental shelf, where tsunami currents are sufficiently larger than background currents (e.g., $> 0.15 - 0.20$ m/s). By contrast, the algorithm proposed by Grilli et al. (2015a), which is being tested here on a realistic case study, takes advantage of the high correlation of time-shifted tsunami currents along a wave ray (Fig. 4c) and of corresponding time-shifted time series of radar signal, to detect tsunami arrival in deeper water as a change in pattern of radar signal correlations. Hence this does not require tsunami currents to reach large values to be detectable. Applying this algorithm for idealized tsunami wave trains and bathymetry, but in the presence of noise and background current, Grilli et al. (2015a) showed that the arrival of tsunami currents as low as background values of 0.05-0.1 m/s could be inferred, and thus tsunami detection could take place in deeper water beyond the continental shelf.

HF radar simulator

We simulate tsunami detection by HF radar using the backscattering model (a.k.a. HF radar simulator) of Grilli et al. (2015a), which accounts for the presence of a time varying surface current in a random sea state. A summary of the main first-order equations of the model is given below; details and second-order equations can be found in reference.

The total surface current over the radar sweep area is assumed to be the sum of: (i) a spatially variable, but nearly stationary at the time scale of radar data acquisition ($> \mathcal{O}(T_i)$) residual (mesoscale) current, $\boldsymbol{U}_0(\boldsymbol{R})$; and (ii) a spatially and temporally varying current, $\boldsymbol{U}_t(\boldsymbol{R},t)$ induced by the tsunami wave train (e.g., Eq. (1)), computed here with FUNWAVE-TVD); hence, $\boldsymbol{U}(\boldsymbol{R},t) = \boldsymbol{U}_0(\boldsymbol{R}) + \boldsymbol{U}_t(\boldsymbol{R},t)$. The residual current, although stationary, is spatially variable in a way that depends on local and synoptic environmental oceanic conditions; in a specific case such as off of Vancouver Island, this current could be obtained from HF radar measurements made over the sweep area prior to tsunami arrival, but this will not even be necessary to apply the proposed tsunami detection algorithm. Because the radar signal is simulated over cells of varying size (Fig. 5b), the tsunami-induced currents computed over the finest grid G3 are spatially averaged over each radar cell (e.g., Fig. 2c), and projected in the radar direction, before being used in the radar simulator.

Assuming a small steepness, the surface elevation of random ocean waves is represented by a second-order perturbation expansion, $\eta(\boldsymbol{R},t) = \eta_1(\boldsymbol{R},t) + \eta_2(\boldsymbol{R},t)$, with,

$$\eta_1(\boldsymbol{R},t) = \sum_{\varepsilon=\pm 1} \int a^{\varepsilon}(\boldsymbol{K})\, e^{\mathrm{i}(\boldsymbol{K}.\boldsymbol{R} - \varepsilon\Omega(\boldsymbol{K},\boldsymbol{R},t)t)}\, \mathrm{d}\boldsymbol{K}, \tag{5}$$

where the integration is carried out over the wavenumber vectors, $\boldsymbol{K} = (K_x, K_y) = K(\cos\theta, \sin\theta)$, and wave harmonic amplitudes are given by,

$$a^{\varepsilon}(\boldsymbol{K}) = \frac{1}{\sqrt{2}} \sqrt{\Psi(\varepsilon\boldsymbol{K})}\, Z^{\varepsilon}(\boldsymbol{K}), \tag{6}$$

with Ψ the directional wave energy density spectrum and $Z^{\varepsilon}(\boldsymbol{K})$ a complex normal variable (with unit variance and zero mean), independent for each wave harmonic. The angular frequency of each wave component, $\Omega(\boldsymbol{K},\boldsymbol{R},t)$, is modulated by the surface current $\boldsymbol{U}(\boldsymbol{R},t)$. Assuming that the tsunami current is slowly varying in time at the scale of ocean waves, i.e., the tsunami characteristic period, $T_t \gg T_p$, the peak spectral wave period, and that waves are in the deep water regime, we have,

$$\Omega(\boldsymbol{K},\boldsymbol{R},t)\, t = (\Omega_g + \boldsymbol{K}.\boldsymbol{U}_0(\boldsymbol{R}))\, t + \int_0^t \boldsymbol{K}.\boldsymbol{U}_t(\boldsymbol{R},\tau)\mathrm{d}\tau, \tag{7}$$

where the integral is a memory term representing the cumulative effects of the tsunami current on the instantaneous wave angular frequency, and, $\Omega_g = \sqrt{gK}$ is the linear angular wave frequency in deep water. Details of $\eta_2(\boldsymbol{R},t)$ can be found in reference.

Here, we simulate fully developed sea states represented by a Pierson-Moskowitz (PM) directional wave energy density spectrum $\Psi(K_x, K_y)$, parametrized as a function of U_{10} and with a standard asymmetric angular spreading function, allowing to model a fraction ξ of wave energy

associated with waves propagating in the direction opposite to the dominant wind direction (see details in Grilli et al. (2015a)). For instance, for $U_{10} = 10$ m/s, $s = 5$, and $\xi = 0.1$, we find a sea state with significant wave height, $H_s = 1.71$ m, peak spectral wavelength $L_p = 127.4$ m and, assuming deep water, peak period $T_p = 9.04$ s.

In a monostatic radar configuration, radar cells are identified by their range vector $\boldsymbol{R}$, centered on the radar (or range R and radar steering angle ϕ_r). The Bragg vector, $\boldsymbol{K}_B$ is defined to point in the radar direction of observation, with $K_B = (2\pi/L_B)$. Up to second-order, the unattenuated backscattered radar signal is denoted by, $\mathrm{S}(t) = \mathrm{S}^1(t) + \mathrm{S}^2(t)$, with,

$$\mathrm{S}^1(t) = \sqrt{2} K_B^2 \sum_{\varepsilon=\pm 1} \sqrt{\Psi(\varepsilon \boldsymbol{K}_B)} e^{-\mathrm{i}\varepsilon\Omega_B t} Z^{\varepsilon}(\boldsymbol{K}_B) \tag{8}$$

where Z^{ε} again denotes a complex normal variable (with unit variance and zero mean), the factor $\sqrt{2}K_B^2$ ensures consistency with the Doppler spectrum definition, and Ω_B is obtained from the wave dispersion relationship in the presence of a current (Eq. (7)). The expression for the second-order signal $\mathrm{S}^2(t)$ can be found in reference. Note that, $\Psi(K) \sim K^{-4}$ for a typical ocean wave spectrum, and hence the magnitude of the unattenuated backscattered radar signal, $\mathrm{S}(t) \sim K_B^2 \sqrt{(\Psi(K_B))}$, is nearly independent from the radar frequency.

Accounting for effects of attenuation with range and environmental noise, the radar signal received from each cell is finally modeled as,

$$\mathrm{V}(t) = \mathscr{A}\,\mathrm{S}(t) + \mathscr{N}(t) \quad \text{with} \quad \mathscr{A}(R) = |\mathrm{F}(R)|^2 R^{-2} \sqrt{\Delta\mathbb{S}}, \tag{9}$$

a geometric attenuation factor function of range R and $\mathscr{N}$ the environmental noise, detailed below. F represents the EMW attenuation by the ocean surface, which is computed here with the GRwave model, as a function of the WERA radar frequency (Grosdidier et al., 2014). We note that attenuation is a strongly decreasing function of both range and frequency (for instance increasing the radar frequency from 4.5 to 13.5 MHz increases $|\,\mathrm{F}(R)\,|$ by a factor of 5 or so at 100 km, and thus the received radar signal attenuation by a factor of 25 or so). Environmental noise is modeled in each cell as an independent complex Gaussian distribution with constant standard deviation σ_N,

$$\mathscr{N}(t) = \sigma_N \{\mathscr{G}_t^R(0,1) + \mathrm{i}\mathscr{G}_t^I(0,1)\}, \tag{10}$$

where t indicates that different Gaussian random values with unit standard deviation and zero mean $[\mathscr{G}_t^R(0,1), \mathscr{G}_t^I(0,1)]$ are being generated for each time t. Since noise is not affected by range, Eq. (9) implies that the radar signal-to-noise ratio (SNR) gradually decreases with range, until the signal becomes undetectable from the noise, which sets the effective radar measuring range (85 km for the WERA radar). Here, we use the same σ_N value as in Grilli et al. (2015a), which was based on HF radar experiments done in the Mediterranean sea, for normal temperature and pressure conditions; in future work, σ_N will be adjusted using site specific values of the SNR for the WERA radar deployed offshore of Tofino, once enough measurements are available for the area.

With an integration time T_i, the (non-normalized) radar Doppler spectrum is calculated at time t_s (with $\Delta t_s \le T_i$) as the mean square of the modulus of the Fourier transform of the received radar signal $\mathrm{V}(t)$, centered on its mean, over a finite time window $[t_s - T_i/2, t_s + T_i/2]$, that is,

$$\mathrm{I}(f_D, t_s) = \frac{1}{T_i} \left| \int_{t_s - \frac{T_i}{2}}^{t_s + \frac{T_i}{2}} \mathrm{V}(\tau)\, \mathrm{e}^{2i\pi f_D \tau} \mathrm{d}\tau \right|^2, \tag{11}$$

with f_D denoting a set of discrete Doppler frequencies (with $\omega_D = 2\pi f_D$). If the received radar signal is simulated/(recorded) at a constant temporal sampling rate $\Delta t = T_i/N$, Eq. (11) can be easily computed as a summation from $-N/2$ to $N/2$.

Given a directional wave energy density spectrum $\Psi(\boldsymbol{K})$ and sets of random functions $Z^{\varepsilon}(\boldsymbol{K})$ (representing random wave phases) and $\mathscr{G}_t$ (used to simulate noise in each cell), time series of the received signal and corresponding Doppler spectra can be simulated for each radar cell by applying Eqs. (8) to (11), in the presence of cell-averaged radial surface currents $\overline{U_r}(\boldsymbol{R}, t)$. More details can be found in Grilli et al. (2015a).

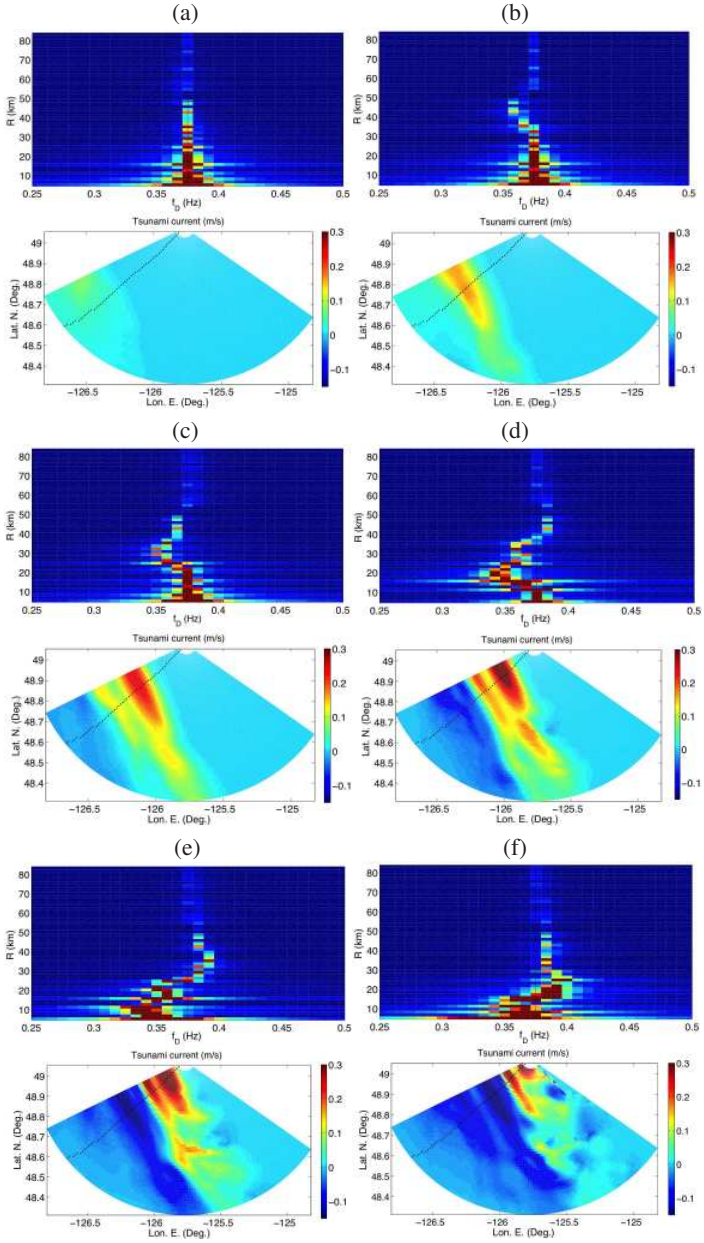

Fig. 6: Case study for SAFRR seismic tsunami source in SSZ. Doppler spectra (first-order) simulated for $T_i = 120$ s (top panels; color scale in Db) and tsunami radial current (bottom panels), in cells aligned along the same wave ray (solid black line in bottom panels and see Fig. 5b) in radar sweep area, at $t =$ (a) 1h42'; (b) 1h49'; (c) 1h56'; (d) 2h03'; (e) 2h10'; (f) 2h17'. Only one side (with positive frequencies) of Doppler spectra is shown, centered on the Bragg frequency $f_B = 0.375$ Hz. Tsunami currents shift this frequency by $\Delta f_B = \pm\,|\,U_{tr}\,|\,/L_B$.

Application of algorithms for tsunami detection to SSZ tsunami

We apply the radar simulator Eqs. (5)-(10) to the WERA radar sweep area off of Tofino (Fig. 5b), assuming a local wind speed $U_{10} = 10$

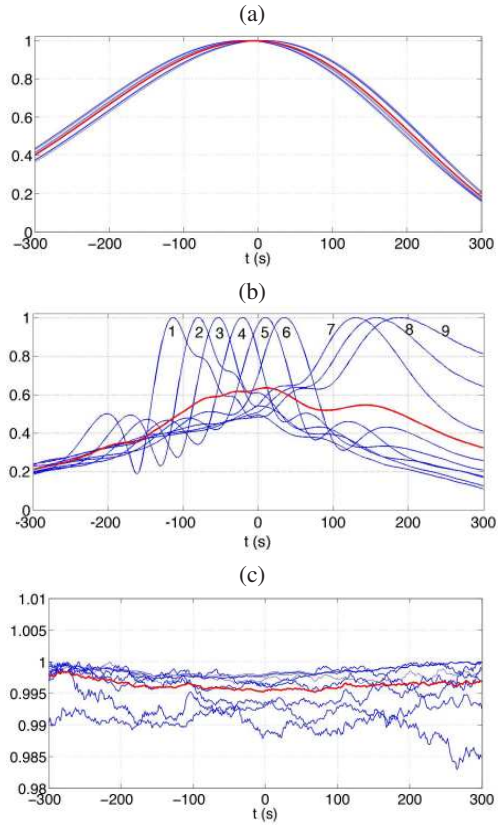

Fig. 7: Time correlations, as a function of additional time lag Δt, between radar cell $q = 4.5$ (in between 4 and 5; 39 km range), and $p = 1,...9$ (3 to 72 km range) aligned along the same wave ray (Fig. 4b), time-shifted by the long wave propagation time $t_{p4.5}$ from cell p to 4.5 of: (a) spatially-averaged radial tsunami currents U_r (Fig 4c); and analytical radar signals simulated with (b) and without (c) tsunami current. Red lined are cell/range averages of each correlation. Correlations use $T_c =$ 600 s, centered on tsunami front arrival time at cell 4.5, $t = 6,240$ s.

m/s, no background current to start with, and using time series of cell-averaged radial tsunami currents $\overline{U_{tr}}(\boldsymbol{R},t)$ calculated for the SSZ tsunami from FUNWAVE-TVD's computations (e.g., Fig. 4b). We simulate time series of received radar signal $\mathrm{V}_p(t)$ in each radar cell p and, based on these, time-dependent Doppler spectra $\mathrm{I}(f_D,t_s)$ (Eq. (11)).

Figure 6 shows snapshots of both tsunami surface current and corresponding Doppler spectra computed for cells aligned along the wave ray shown in Fg. 5b, between 1h42' and 2h16' (6,120 to 8,160 sec) into the event. These results show that a direct inversion of the propagating tsunami currents based on the oscillatory shift induced in Doppler spectra (referred to by Grilli et al. (2015a) as Tsunami Detection Algorithm 1; TDA1) would become effective at about a 45 km range. This corresponds to cell 5 in Fig. 5b, for which Fig. 4b shows that the maximum cell-averaged radial current is just above 0.2 m/s; however, the integration time $T_i = 120$ sec used to compute Doppler spectra means the radar signal is based on currents that are also averaged over this time, $\widetilde{\overline{U_{tr}}}(\boldsymbol{R},t)$, which reduces current magnitude (here, just below 0.2 m/s). Assuming the tsunami is detected immediately upon reaching Station 5, from this location of detection, the tsunami would reach the shore within 20-25 min, which only offers very low warning time. This is consistent with the conclusion of the idealized study of Grilli et al. (2015a), that TDA1 is only reliable for $|\,\widetilde{\overline{U_{tr}}}\,| > 0.15-0.20$ m/s.

We now evaluate the performance of the Tsunami Detection Algorithm 2 (TDA2) proposed by Grilli et al. (2015a) on the basis of time-shifted correlations of radar signal. As already pointed out , once shifted by the long wave propagation time Δt_{pq} between two cells p and q located along the same wave ray, Fig. 4c showed that tsunami radial currents appear to be highly correlated. This is verified here by computing the correlation of time series of time-shifted currents (subscript r was dropped for simplicity),

$$\mathrm{corr}\{\overline{U}_{tq}(t-\Delta\tau),\overline{U}_{tp}(t)\} = \frac{1}{T_c}\int_{t-\frac{T_c}{2}}^{t+\frac{T_c}{2}} \overline{U}_{tq}(\tau-\Delta\tau)\overline{U}_{tp}(\tau)\mathrm{d}\tau \qquad (12)$$

as a function of an additional time lag Δt, where T_c is the correlation time (here 600 sec but nearly similar results are obtained for 300 s), which unlike T_i can be $\gg T_t$. Fig. 7a shows that such correlations, calculated between station $q = 4.5$ (i.e., in between stations 4 and 5; 39 km range) and stations $p = 1,...9$ (3 to 72 km range) (Figs. 5b) are maximum near the zero time lag, and drop on either side of it (for positive or negative time lags). Because the radar signal is modulated by surface currents, we expect to observe similarly high values of the correlations between two cells, near the zero time lag, for the time shifted received radar signal,

$$\mathrm{corr}\{\mathrm{V}_q(t-\Delta\tau),\mathrm{V}_p(t)\} = |\,\frac{1}{T_i}\int_{t}^{t+T_i} \mathrm{V}_q(\tau-\Delta\tau)\,\mathrm{V}_p^*(\tau)\mathrm{d}\tau\,|, \qquad (13)$$

due to the presence of the highly correlated tsunami current. By contrast these correlations should be flat as a function of time lag in the absence of a tsunami current (and this will hold true in the presence of uncorrelated background currents). This pattern is indeed observed in Figs. 7b and 7c, for correlations at stations 1 to 9, with and without current, respectively. [Note that, to reduce high frequency noise in correlations, these are computed on the analytical radar signals, which are calculated, for simulated or measured signals, by applying a Fourier transform (FT) to the signal, removing the negative frequencies, and applying an inverse FT; see details in Grilli et al. (2015a).] Correlations averaged over cells 1 to 9 are also plotted in Fig. 7 as thick red lines; in Figs. 7a and b, these are clearly peaked near the zero time lag in the presence of a tsunami current, but flat in Fig. 7c in the absence of a current.

Due to lack of space, we do not show results in the presence of a random background current, but these will be shown at the conference and confirm that currents from both a spatially varying (but nearly stationary at the considered scales) mesoscale current and local effects of environmental conditions (e.g., wind), have no correlation between two cells selected on a wave ray (and more particularly so when shifted in time by Δt_{pq}), and hence do not affect correlations in Eqs. (12) and (13). Thus, only the spatially coherent surface current caused by a tsunami affects correlations of the radar signal shifted by the long wave propagation time. This property is well supported in our numerical simulations and justifies why a much weaker, but spatially coherent, tsunami current can be detected by this algorithm, even in the presence of a background current of similar or even larger magnitude. This change in average correlation pattern over a series of cells can be dynamically evaluated when processing the radar signal in real time and used to detect the arrival of a tsunami.

It should be finally emphasized that, unlike with TDA1, with TDA2 we do not need to estimate currents by inverting the Doppler spectra and hence limitations in such an inversion, in terms of integration time $T_i \ll T_t$, resolution $\Delta U_r \propto 1/T_i$, and the need for currents to be $> 0.15-0.20$ m/s, do not apply. We see for instance that correlations between cell 4.5 and 1 to 9 in Fig. 7 all have a similar pattern, whereas the current magnitude is less than 0.05 m/s at station 9, in a 500 m depth and reaches nearly 0.3 m/s in station 2, in a 50 m depth. This confirms the conclusions of Grilli et al. (2015a), but here this is based on a realistic case study.

CONCLUSIONS

The detection of tsunamis by HF radars, based on a direct inversion of tsunami currents from the radar signal Doppler spectra (referred to as

algorithm TDA1), is typically limited to areas where such currents are large enough as compared to background currents (i.e., $> 0.15 - 0.2$ m/s), hence, to shallow water and the continental shelf. To overcome this limitation, Grilli et al. (2015a) proposed a new detection algorithm (TDA2) based on observing changes in pattern of correlations between two radar cells, of time series of radar signal shifted by the tsunami propagation time between the cells; TDA2 was validated on case studies with idealized tsunami wave trains and bathymetry. Here, we confirmed that TDA2 is also applicable to realistic tsunami case studies performed off of Vancouver Island, BC, for an incident tsunami from a Semidi SSZ M_w 9.1 event. Time-shifted correlations of radar signal between pairs of radar cells aligned along the same wave ray, computed for simulated tsunami currents, showed that TDA2 can detect the effects on correlations of radar signal of currents as low as 0.05 m/s; hence, this makes tsunami detection possible in deeper water, beyond the continental shelf.

TDA2 can be easily implemented in a radar system, in a real time tsunami detection mode (rather than simulation mode) for which the radar signal is continuously measured (rather than computed with a radar simulator), processed in all the radar cells (Fig. 5b), and time-shifted correlations are dynamically calculated between all pair of cells located along a large number of pre-computed wave rays (Fig. 5b). To detect tsunamis from expected (e.g., seismic) or unknown (SMF) tsunami sources, a series of wave rays can be pre-computed for tsunamis incident from a range of potential directions, based on bathymetry, and used in the algorithm. Applying TDA2, the appearance of a peaked correlation between time series of time-shifted radar signals, in pairs of cells located along the same wave ray (for a single pair of cell or averaged over a few cells, from offshore to onshore), will indicate that a tsunami is approaching the radar. In the range of periods/time scales that are considered here, there is indeed no other geophysical phenomenon that can create long wave trains that are spatially coherent, with a current magnitude sufficient to cause measurable modulations in the HF radar signal. By computing signal correlations in all relevant pairs of cells along one or many wave rays, one can thus track the progression in time of an incoming tsunami by following the locations (front) of peaked correlations (e.g., Fig. 7; this was verified in simulations). In the absence of a spatially coherent current, signal correlations are independent of time lag (i.e., are flat); therefore, a marked difference in correlation pattern around the theoretical long wave propagation time (zero time lag) can be used to specify a tsunami detection threshold for the algorithm.

Acknowledgement: ONC is gratefully acknowledged for providing support for this research, as well as access to their radar system data.

REFERENCES

Abadie, S., Harris, J. C., Grilli, S. T., and Fabre, R. (2012). Numerical modeling of tsunami waves generated by the flank collapse of the Cumbre Vieja Volcano (La Palma, Canary Islands) : tsunami source and near field effects. *J. Geophys. Res.*, 117:C05030.

Barrick, D. E. (1979). A coastal radar system for tsunami warning. *Remote Sensing of Environment*, 8(4):353–358.

Benjamin, L. R., Flament, P., Cheung, K. F., and Luther, D. S. (2016). The 2011 Tohoku tsunami south of Oahu: high-frequency Doppler radio observations and model simulations of currents. *J. Geophys. Res. (publ. online)*, pages 1–29.

Dean, R. G. and Dalrymple, R. A. (1984). *Water Wave Mechanics for Engineers and Scientists*. Prentice-Hall.

Dzvonkovskaya, A. (2012). Ocean surface current measurements using HF radar during the 2011 Japan tsunami hitting Chilean coast. In *Geoscience and Remote Sensing Symp. (IGARSS), 2012 IEEE Intl.*, pages 7605–7608. IEEE.

Dzvonkovskaya, A., Gurgel, K.-W., Pohlmann, T., Schlick, T., and Xu, J. (2009). Simulation of tsunami signatures in ocean surface current maps measured by HF radar. In *OCEANS 2009-EUROPE*, pages 1–6. IEEE.

Fine, I., Rabinovich, A., Bornhold, B., Thomson, R., and Kulikov, E. (2005). The Grand Banks landslide-generated tsunami of November 18, 1929: preliminary analysis and numerical modelling. *Mar. Geol.*, 215:45–57.

Grilli, S. T., Dubosq, S., Pophet, N., Pérignon, Y., Kirby, J., and Shi, F. (2010). Numerical simulation and first-order hazard analysis of large co-seismic tsunamis generated in the Puerto Rico trench: near-field impact on the North shore of Puerto Rico and far-field impact on the US East Coast. *Natural Hazards and Earth System Sciences*, 10:2109–2125.

Grilli, S. T., Grosdidier, S., and Guérin, C.-A. (2015a). Tsunami detection by High Frequency Radar beyond the continental shelf. I. Algorithms and validation on idealized case studies. *Pure and Applied Geophysics*, pages 1–40 (published online 10/28/15).

Grilli, S. T., Harris, J. C., Tajalli-Bakhsh, T., Masterlark, T. L., Kyriakopoulos, C., Kirby, J. T., and Shi, F. (2013). Numerical simulation of the 2011 Tohoku tsunami based on a new transient FEM co-seismic source: Comparison to far- and near-field observations. *Pure and Applied Geophysics*, 170:1333–1359.

Grilli, S. T., Ioualalen, M., Asavanant, J., Shi, F., Kirby, J. T., and Watts, P. (2007). Source constraints and model simulation of the December 26, 2004 Indian Ocean tsunami. *Journal of Waterway Port Coastal and Ocean Engineering*, 133(6):414–428.

Grilli, S. T., O'Reilly, C., Harris, J., Tajalli-Bakhsh, T., Tehranirad, B., Banihashemi, S., Kirby, J., Baxter, C., Eggeling, T., Ma, G., and Shi, F. (2015b). Modeling of SMF tsunami hazard along the upper US East Coast: Detailed impact around Ocean City, MD. *Natural Hazards*, 76(2):705–746.

Grosdidier, S., Forget, P., Barbin, Y., and Guerin, C.-A. (2014). HF bistatic ocean Doppler spectra: Simulation versus experimentation. *IEEE Trans. Geosci. and Remote Sens.*, 52(4):2138–2148.

Gurgel, K.-W., Dzvonkovskaya, A., Pohlmann, T., Schlick, T., and Gill, E. (2011). Simulation and detection of tsunami signatures in ocean surface currents measured by HF radar. *Ocean Dynamics*, 61(10):1495–1507.

Heron, M. L., Prytz, A., Heron, S. F., Helzel, T., Schlick, T., Greenslade, D. J., Schulz, E., and Skirving, W. J. (2008). Tsunami observations by coastal ocean radar. *International Journal of Remote Sensing*, 29(21):6347–6359.

Hinata, H., Fujii, S., Furukawa, K., Kataoka, T., Miyata, M., Kobayashi, T., Mizutani, M., Kokai, T., and Kanatsu, N. (2011). Propagating tsunami wave and subsequent resonant response signals detected by HF radar in the Kii Channel, Japan. *Estuarine, Coastal and Shelf Science*, 95(1):268–273.

Insua, T., Grilli, A. R., Grilli, S. T., Shelby, M., Wang, K., Gao, D., Cherniawsky, J., Harris, J. C., Heesemann, M., McLean, S., and Moran, K. (2015). Preliminary tsunami hazard assessment in British Columbia, Canada. *EOS Trans. AGU*, 96(52):Fall Meet. Suppl., Abstract NH23C–1890.

Ioualalen, M., Asavanant, J., Kaewbanjak, N., Grilli, S. T., Kirby, J. T., and Watts, P. (2007). Modeling the 26th December 2004 Indian Ocean tsunami: Case study of impact in Thailand. *J. Geophys. Res.*, 112:C07024.

Kirby, J. T., Shi, F., Tehranirad, B., Harris, J. C., and Grilli, S. T. (2013a). Dispersive tsunami waves in the ocean: Model equations and sensitivity to dispersion and Coriolis effects. *Ocean Modeling*, 62:39–55.

Kirby, S., Scholl, D., Von Huene, R., and Wells, R. (2013b). Alaska earthquake source for the SAFRR tsunami scenario. Technical Report USGS Report, 2013, U.S. Geological Survey Open-File . http://pubs.usgs.gov/of/2013/1170/b/, The SAFRR (Science Application for Risk Reduction) Tsunami Scenario.

Lipa, B., Barrick, D., Saitoh, S.-I., Ishikawa, Y., Awaji, T., Largier, J., and Garfield, N. (2011). Japan tsunami current flows observed by HF radars on two continents. *Remote Sensing*, 3(8):1663–1679.

Lipa, B., Isaacson, J., Nyden, B., and Barrick, D. (2012). Tsunami arrival detection with high frequency (HF) radar. *Remote Sensing*, 4(5):1448–1461.

Lipa, B. J., Barrick, D. E., Bourg, J., and Nyden, B. B. (2006). HF radar detection of tsunamis. *Journal of Oceanography*, 62(5):705–716.

Shi, F., Kirby, J. T., Harris, J. C., Geiman, J. D., and Grilli, S. T. (2012). A high-order adaptive time-stepping TVD solver for Boussinesq modeling of breaking waves and coastal inundation. *Ocean Modeling*, 43-44:36–51.

Tappin, D. R., Grilli, S. T., Harris, J. C., Geller, R. J., Masterlark, T., Kirby, J. T., Shi, F., Ma, G., Thingbaijamg, K., and Maig, P. (2014). Did a submarine landslide contribute to the 2011 Tohoku tsunami ? *Marine Geol.*, 357:344–361.

Tappin, D. R., Watts, P., and Grilli, S. T. (2008). The Papua New Guinea tsunami of 1998: anatomy of a catastrophic event. *Natural Hazards and Earth System Sciences*, 8:243–266.

Tehranirad, B., Harris, J., Grilli, A., Grilli, S., Abadie, S., Kirby, J., and Shi, F. (2015). Far-field tsunami hazard in the north Atlantic basin from large scale flank collapses of the Cumbre Vieja volcano, La Palma. *Pure and Applied Geophysics*, 172(12):3,589–3,616.

Tehranirad, B., Shi, F., Kirby, J. T., Harris, J. C., and Grilli, S. T. (2011). Tsunami benchmark results for fully nonlinear Boussinesq wave model FUNWAVE-TVD, Version 1.0. Technical Report No. CACR-11-02, Univ. of Delaware.

Thomson, R. E., Rabinovich, A. B., Fine, I. V., Sinnott, D. C., McCarthy, A., Sutherland, N. A. S., and Neil, L. K. (2009). Meteorological tsunamis on the coasts of British Columbia and Washington. *Physics and Chemistry of the Earth Parts A/B/C*, 34(17):971–988.